

Experimental analysis and visualization of spatiotemporal patterns in spouted fluidized beds

Antonio Palacios^{a)}

Nonlinear Dynamics Group, Department of Mathematics & Statistics, San Diego State University, San Diego, California 92182

Charles Finney^{b)}

Engineering Science and Technology Division, Oak Ridge National Laboratory, Oak Ridge, Tennessee 37831

Paul Cizmas^{c)}

Department of Aerospace Engineering, Texas A&M University, College Station, Texas 77843

Stuart Daw^{d)}

Engineering Science and Technology Division, Oak Ridge National Laboratory, Oak Ridge, Tennessee 37831

Thomas O'Brien^{e)}

Department of Energy, National Energy Technology Laboratory, Morgantown, West Virginia 26507-0880

(Received 17 October 2003; accepted 19 March 2004; published online 21 May 2004)

A numerical characterization based on experimental data of the spouting regime in a two-dimensional fluidized bed is presented. The aspect ratio of the bed allowed for good visualization of the spouting and solids circulation as the spouting jet gas velocity was varied to highlight the visited bifurcation sequence. Digital video sequences were recorded and then preprocessed for numerical analysis. In this paper, the proper orthogonal decomposition (POD) was applied to these data sets in order to identify and separate the dominant spatial features from the temporal evolution of the spouting dynamics. The results indicate that the overall spatiotemporal dynamics can be captured by a few POD eigenfunctions, and that the POD amplitudes can be used to distinguish between varying degrees of spouting. © 2004 American Institute of Physics. [DOI: 10.1063/1.1739012]

Previous experimental works have revealed that the hydrodynamics of fluidized beds exhibit many features associated with low-dimensional deterministic chaos. Hence, in principle, it should be possible to control the overall patterns of solids mixing, thus altering gas–solids contacting efficiency, by exploiting the sensitivity of the system to small perturbations. In this work, we employ the proper orthogonal decomposition, and experimental data, to identify and extract coherent structures in the spouting dynamics with the purpose of understanding the transitions and response of the bed to changes in parameters, namely, to changes in the spouting jet gas velocity. It is our hope that this work can lead to future low-dimensional models and possible control strategies.

I. INTRODUCTION

Fluidization is a process in which solid particles are suspended in a fluid-like state by a carrier medium, typically air. This phenomenon occurs when the drag forces on the particles from the upward fluid flow exceed gravitational and interparticle forces. Fluidized-bed reactors afford excellent

gas–solid contacting and particle mixing, facilitate the control of highly exothermal reactions, and provide good gas-to-particle and bed-to-wall heat transfer. However, they also have disadvantages, such as a broad residence time distribution of the gas and particles, gas-bypassing in the form of gas bubbles, jets and channeling, the erosion of bed internals, and the attrition of the bed material. Common engineering applications of fluidization technology include coal combustion, the production of polyethylene, and the cracking of hydrocarbons. Fluidization is in many ways related to the field of granular dynamics but offers a set of unique features and challenges because of the way the particles are agitated.

Fluidization occurs in many different dynamical regimes, depending on a variety of factors such as particle size, density and geometry, vessel size and geometry, the gas-distribution system, and gas flow rate. A very common regime is bubbling, in which voids (“bubbles”) form in the granular bed and rise with a vigorous motion. In rising, these bubbles entrain particles upward with them and thus create large-scale patterns of solids circulation. Bubbling occurs with many common solids of industrial importance and is a fairly well-understood and widespread regime. Typically, bubbling fluidized-bed vessels are cylindrical or rectangular in cross section with a flat bottom plate with some arrangement of multiple gas inflow orifices.

Some particle types, based on their (typically large) size or density, are difficult to fluidize in the bubbling regime. Instead, solids circulation for chemical reaction or heat trans-

^{a)}Electronic mail: palacios@euler.sdsu.edu

^{b)}Electronic mail: finneyc@ornl.gov

^{c)}Electronic mail: cizmas@tamu.edu

^{d)}Electronic mail: dawcs@ornl.gov

^{e)}Electronic mail: thomas.obrien@netl.doe.gov

fer may be achieved by operating in the spouting regime. Typically, spouted beds are cylindrical in cross section but have an inverted conical base with a single gas input at the vertex; some spouting vessels have flat bases. With sufficient gas flow through this orifice, a strong, coherent gas jet flows up the vessel central axis, and particles are entrained within this jet at great velocity upwards. At the surface of the bed, the gas escapes to the exhaust system, but particles follow a ballistic trajectory and rain back down to the bed surface or side walls. They then migrate downwards until they are entrained in the upward gas flow again. The spouting regime in some respects is not as well understood and widespread as the bubbling regime but has significant industrial importance and relevance.

Depending on the spouting gas velocity, bed depth, and particle characteristics, the gas jet within the bed and spout of particles above the bed display different degrees of stability. (In some ways, this is reminiscent of the dynamics of water fountains.) Understanding the spatial and temporal behavior of the jet and spout is important because well-controlled conditions can maximize the efficiency of fluid-particle contacting and particle mixing while mitigating their negative effects. This understanding can be achieved with good physical characterization and the development of numerical physical models. Of particular interest is the development of lower-order models which can be executed quickly, in or around real time, to aid process development and design. One of the aims of this work is to investigate the existence of coherent structures in the spouting dynamics, which may then lead to more accurate low-dimensional models.

In the last decade, studies by Skrzyzke *et al.*,¹ Daw *et al.*,^{2,3} Daw and Halow,^{4,5} Schouten *et al.*,^{6–8} and vander Stappen *et al.*^{9–11} have shown that the hydrodynamics of fluidized beds exhibit many features associated with low-dimensional deterministic chaos. Then, in principle, one should be able to control the hydrodynamics of fluidization behavior by exploiting the sensitivity of the system to small perturbations. Such control strategy has not been developed yet, mainly because the use of chaos-based methods in fluidization has gained attention only in recent years.^{12–14} Additionally, the lack of realistic low-dimensional models for bubbling and spouting behavior has limited the progress of chaos-based control strategies. More recently, however, computational models for simulating gas–solid interactions have also been developed. Such models are derived from the conservation laws for mass, momentum, energy, and species. The resulting governing equations consist of large and strongly coupled systems of partial differential equations (PDEs).

Due to the high dimensionality of the PDEs, understanding and predicting the spatiotemporal behavior of fluid-particle interactions, using analytical methods, is not feasible. Instead, numerical and laboratory experiments are first conducted to get insight into the complexity of the interactions. In particular, they are used to identify and extract any dominant spatial features that can lead to simplified reduced-order models and to relate these features to specific bifurcation events in the overall dynamics. Numerical simulations

can suffer from limitations on accuracy and excessive computer-time requirements. In order to circumvent these limitations, in this work we identify and extract, directly from the laboratory experiments, the coherent structures that appear at various states of spouting. In particular, a series of well-controlled experiments were conducted using a two-dimensional bed filled with small particles of zircshot (ZrO_2). The uniformly distributed air flow to the bed was maintained just below minimum fluidization. A centerline nozzle was then used to inject a controlled flow of excess air. We then seek to understand any changes in the bed dynamics in response to changes in the velocity of the air flow injected through this nozzle.

The proper orthogonal decomposition method is used to extract the dominant spatial features directly from the experimental data. A predominantly visible coherent structure is the gas jet rising along the centerline and up through the bed surface. An additional significant structure is the arch of the particle fountain above the bed surface. The gas–particle flow within these structures, and at the bed surface, is successfully captured by a few proper orthogonal decomposition (POD) eigenfunctions. Approximately 20 eigenfunctions can account for 80% of the original dynamics. The first two eigenfunctions capture approximately 50% of the behavior. Furthermore, when the air flow velocity is low, the contribution of the first two modes (measured by the POD energy function) is almost equal. As the flow velocity increases, however, the contribution of the second mode decreases and that of higher modes increases.

Our results suggest that a reduced-order model could be constructed, for instance, via Galerkin methods, in which a suitable PDE model is projected onto the POD modes to generate a low-dimensional system of ordinary differential equations. However, we do not attempt such a construction in this work. The reduced order model has the potential to help us further investigate, at near real-time speeds, fluid-particle contacting and how to control the resulting interaction. Understanding this interaction can significantly impact the use of fluidization in engineering applications.

This paper is organized as follows. Section II presents a brief introduction to the fluidization phenomenon. In Sec. III we describe the experimental investigation of spouting dynamics in a fluidized bed. Section IV presents basic properties of the proper orthogonal decomposition relevant to this work. In particular, a theoretical description is provided, followed by a computational implementation for numerical simulations or experimental data. Section V describes the results of applying the proper orthogonal decomposition to experimental data. The results support the existence of low-dimensional dynamics and suggest that building reduced order models via Galerkin methods can be successful. This latter task is part of future work.

II. FLUIDIZED BEDS

Fluidization is the phenomenon in which a bed of solid particles acquires fluid-like properties^{15–18} due to the interstitial upward flow of a fluid through the bed. Fluidized beds normally consist of a vessel containing the solids with a

bottom plate through which the fluidizing medium, usually gas, can be introduced. At low fluid flow rates, the fluid percolates through the void spaces between the solids, which remains a packed bed; the forces acting on the bed due to the flow of the fluid are less than the weight of the bed. When the flow rate is increased over a certain threshold, the minimum fluidization velocity, the solids become levitated due to the interaction between the fluid and the particles and the bed behaves like a fluid. That is, lighter particles float on top of the bed, the surface of the solids bed stays horizontal when its containment vessel is tilted (like water in a glass), and the solids can flow through an opening, such as a valve. This state is called fluidization.

If the fluid flow rate is further increased, a second velocity threshold appears, beyond which voids, shaped like bubbles, form and rise through the bed with vigorous motion and extensive coalescence and splitting.^{19–23} This state is called the bubbling fluidization regime and the threshold velocity at which it first occurs is called the minimum bubbling velocity. The onset of bubble formation depends on the actual type and size of solid particles and on the particle/fluid density ratio. In a bed of coarse particles fluidized by a gas, for example, the onset of bubble formation is approximately the same as the minimum fluidization velocity. But regardless of when bubbles are formed, their vigorous motion, including coalescence and splitting, is important because they affect the efficiency of particle mixing. A bed with uniformly distributed fine bubbles, for instance, will generally lead to a higher chemical conversion than a bed containing a few large bubbles. If the fluid flow rate is increased beyond the terminal velocity of the particles, then the solids would be swept out of the container. If this material is captured and returned to the bed then the unit is operating in the circulating fluidization regime. Of interest in the present work is a highly energetic form of bubbling called spouting. This regime typically occurs when input gas is focused within a small area, such as a single orifice, rather than through a uniform distributor and when the bed depths are shallow. Bubbles are formed from the jet and rise so quickly through the bed that they can merge into a single stream of gas. This jet stream pulls with it particles and actually ejects these particles in a spout above the bed surface, much like a water fountain. Depending on the jet gas velocity, the particle properties, and the bed depth, the spouting dynamics can vary greatly.

Although there can be significant gas bypass in this regime resulting in less gas–solids contacting, this is still an industrially useful and relevant operational state. Additionally, the complexity of the regime yet presence of coherent structures such as the fountain effect makes it an interesting research topic. For more information on the general engineering relevance of fluidization, please consult Ref. 24. The spouting regime specifically is treated in Refs. 25 and 26.

III. THE EXPERIMENTAL SYSTEM

A two-dimensional fluidized bed was constructed at the University of Tennessee for the Oak Ridge National Laboratory using transparent acrylic. The dimensions of the bed were 25.3 cm wide, 1.9 cm deep, and 77.5 cm tall. Metered,

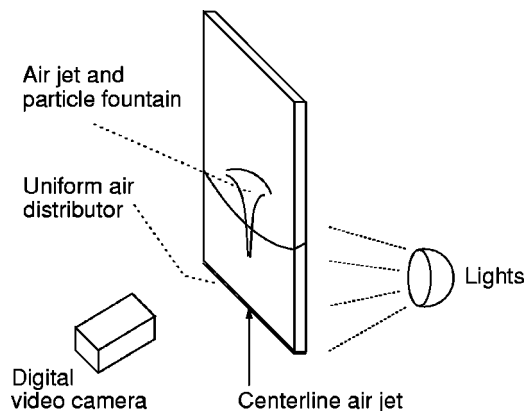


FIG. 1. Schematic diagram of experimental fluidization apparatus.

regulated air was passed through a sintered-metal distributor (with high pressure drop for uniform fluidization and reduction of feedback to the air supply) for the bed-wide fluidization of particles. Additionally, a single square nozzle 0.5 cm to a side was located directly at the vessel centerline flush to the distributor plate, and through this centerline nozzle a controlled flow of air was passed. In the experiments described here, the vessel was filled with 300 μm spherical zirco-shot (ZrO_2) (material density of 5.6 gm/cm^3) to a static depth of 15 cm. Then the bed was uniformly fluidized to around 10 cm/s (below minimum fluidization to avoid free bubbling elsewhere in the bed) to reduce interparticle locking which might inhibit jet dynamics, and the centerline nozzle flow velocity was varied as the experimental parameter. Figure 1 shows a schematic depiction of the final apparatus.

Video images of the spouting dynamics were recorded with a Sony digital video camera located normal to the front surface of the bed. At each unique flow condition, 5 min of video records of the bed front face were recorded at 30 frames/s. The bed was illuminated from the rear face through a translucent sheet of plastic for diffuse background lighting, so that any gas pockets (the jet) occupying a significant proportion of the 1.9 cm vessel depth would show up clearly on the video record. Each frame of video was cropped to a fixed area to remove external features (such as flanges and tubing) not important to the dynamics, interlacing lines removed with a row-wise kernel neighborhood-averaging technique,²⁷ and then converted to grayscale for data analysis. The intent with this video setting was to record global features such as spout height, bed-surface profile, and jet penetration height, with the realization that the limited spatial and temporal resolution might miss certain fine features such as granular flows and fine bubbling in the gas jet.

Additionally, a differential pressure measurement (relative to atmosphere) was obtained from a wall-flush pressure tap along the vessel side wall 7.5 cm above the distributor. The analog voltage signal from a Baratron transducer was bandpass-filtered between 0.1 and 40 Hz (to remove instrument drift and 60 Hz electronic noise contamination) before being digitized with 12 bit precision at 200 samples/s with a Nicolet 440 digitizing oscilloscope. The resulting time series were stored for off-line analysis.

IV. PROPER ORTHOGONAL DECOMPOSITION

The proper orthogonal decomposition is a well-known technique for determining an optimal basis for the reconstruction of a data set.^{28,29} The POD has been used in various disciplines that include fluid mechanics,^{30–32} identification and control in chemical engineering,³³ oceanography,³⁴ image processing,³⁵ and flutter prediction.³⁶ Depending on the discipline, the POD is also known as Karhunen–Loève decomposition, principal components analysis, singular systems analysis, and singular value decomposition. The following reviews the definitions and properties of the proper orthogonal decomposition relevant to this work and discusses how the method can be applied to computer simulations in order to separate spatial and temporal behavior.

A. Theoretical aspects

Let us consider a sequence of numerical and/or experimental observations represented by scalar functions $u(\mathbf{x}, t_i), i = 1, \dots, M$. These functions are assumed to form a linear ($M \neq \infty$) infinite-dimensional Hilbert space L^{237} on a domain D which is a bounded subset of \mathbb{R}^n , and they are parametrized by t_i , which represents time. The time-average of the sequence, defined by

$$\bar{u}(\mathbf{x}) = \langle u(\mathbf{x}, t_i) \rangle = \frac{1}{M} \sum_{i=1}^M u(\mathbf{x}, t_i), \tag{1}$$

is assumed to be zero, without loss of generality. The proper orthogonal decomposition extracts time-independent orthonormal basis functions, $\Phi_k(\mathbf{x})$, and time-dependent orthonormal amplitude coefficients, $a_k(t_i)$, such that the reconstruction

$$u(\mathbf{x}, t_i) = \sum_{k=1}^M a_k(t_i) \Phi_k(\mathbf{x}), \quad i = 1, \dots, M \tag{2}$$

is optimal in the sense that the average least square truncation error

$$\varepsilon_m = \left\langle \left\| u(\mathbf{x}, t_i) - \sum_{k=1}^m a_k(t_i) \Phi_k(\mathbf{x}) \right\|^2 \right\rangle \tag{3}$$

is a minimum for any given number $m \leq M$ of basis functions over all possible sets of orthogonal functions. Here $\|\cdot\|$ is the L^2 -norm $\|f\|^2 = (f, f)$, where (\cdot, \cdot) denotes the standard Euclidean inner product. The functions $\Phi_k(\mathbf{x})$ are called *empirical eigenfunctions*, *coherent structures*, or *POD modes*.

The optimality property (3) is equivalent to finding functions Φ that maximize the normalized average projection of u onto Φ ,

$$\max_{\Phi \in L^2(D)} \frac{|(u, \Phi)|^2}{\|\Phi\|^2}, \tag{4}$$

where $|\cdot|$ denotes the modulus. The optimum condition (4) reduces to the eigenvalue problem³⁰

$$\int_D \langle u(\mathbf{x}) u^*(\mathbf{y}) \rangle \Phi(\mathbf{y}) d\mathbf{y} = \lambda \Phi(\mathbf{x}), \tag{5}$$

where $\mathbf{x}, \mathbf{y} \in D$. Consequently, the optimal basis functions $\{\Phi_k\}$ are the eigenfunctions of the integral equation (5), whose kernel is the averaged *autocorrelation* function

$$\langle u(\mathbf{x}) u^*(\mathbf{y}) \rangle \equiv R(\mathbf{x}, \mathbf{y}).$$

In practice the state of a numerical model is only available at discrete spatial grid points, so that the observations that form the data set are vectors rather than continuous functions. In other words, $D = (x_1, x_2, \dots, x_N)$, where x_j is the j th grid point and $u(\mathbf{x}, t_i)$ is the vector $\mathbf{u}_i = [u(x_1, t_i), u(x_2, t_i), \dots, u(x_N, t_i)]^T$. The data set can be obtained from numerical simulation, experimental investigation, or a combination of the numerical and experimental results. In the discrete case, the autocorrelation function is replaced by the tensor product matrix

$$R(\mathbf{x}, \mathbf{y}) = \frac{1}{M} \sum_{i=1}^M \mathbf{u}_i \mathbf{u}_i^T. \tag{6}$$

More important, it can also be shown that the eigenvectors of the $R(\mathbf{x}, \mathbf{y})$ matrix yield the eigenfunctions $\Phi_k(\mathbf{x})$, which can be computed with the algorithm presented in Sec. IV B.

B. Computational implementation: Method of snapshots

A popular technique for finding the eigenvectors of Eq. (6) is the *method of snapshots* developed by Sirovich.³⁸ It was introduced as an efficient method when the resolution of the spatial domain (N) is higher than the number of observations (M). The method of snapshots is based on the fact that the data vectors, \mathbf{u}_i , and the eigenvectors Φ_k , span the same linear space.^{31,38} This implies that the eigenvectors can be written as a linear combination of the data vectors,

$$\Phi_k = \sum_{i=1}^M v_i^k \mathbf{u}_i, \quad k = 1, \dots, M. \tag{7}$$

After substitution in the eigenvalue problem, $R(\mathbf{x}, \mathbf{y}) \Phi(\mathbf{y}) = \lambda \Phi(\mathbf{x})$, the coefficients v_i^k are obtained from the solution of

$$C \mathbf{v} = \lambda \mathbf{v}, \tag{8}$$

where $\mathbf{v}^k = (v_1^k, \dots, v_M^k)$ is the k th eigenvector of Eq. (8), and C is a symmetric $M \times M$ matrix defined by $[c_{ij}] = (1/M) (\mathbf{u}_i, \mathbf{u}_j)$. Here (\cdot, \cdot) denotes the standard vector inner product, $(\mathbf{u}_i, \mathbf{u}_j) = u(x_1, t_i) u(x_1, t_j) + \dots + u(x_N, t_i) u(x_N, t_j)$. In this way the eigenvectors of the $N \times N$ matrix R (6) can be found by computing the eigenvectors of an $M \times M$ matrix C (8), a preferable task if $N \gg M$. The results presented in Sec. V were obtained with an implementation of the method of snapshots. An iterative QR method³⁹ was used to compute the eigenvectors of the symmetric matrix C from Eq. (8).

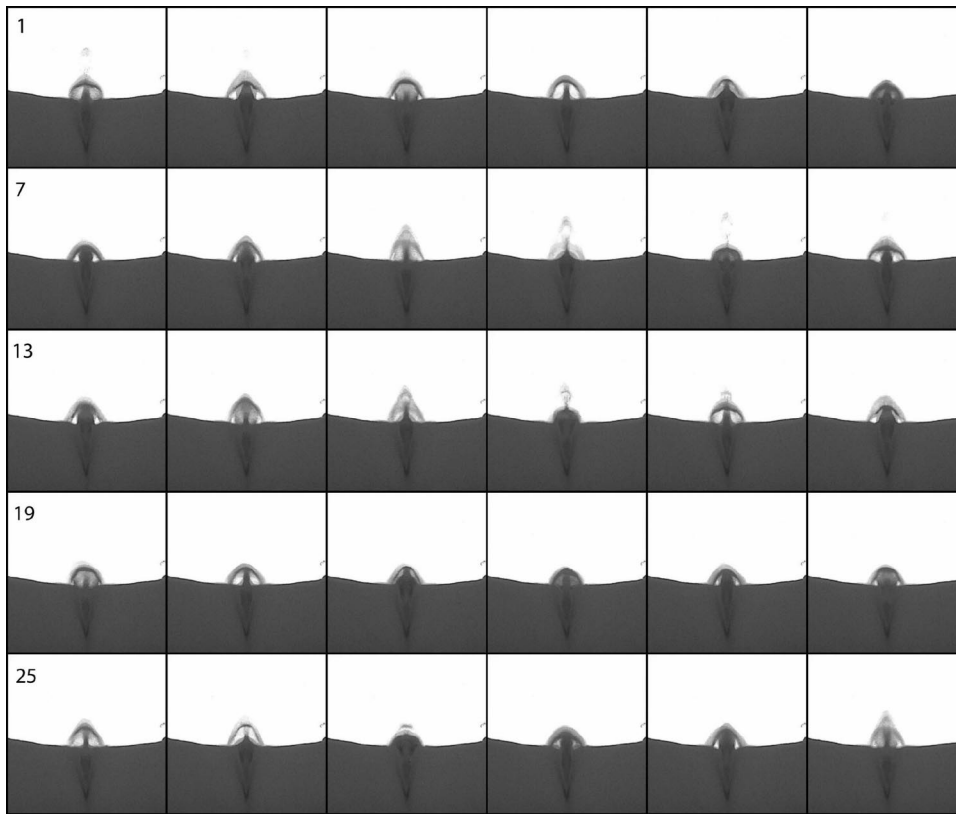


FIG. 2. Montage of spatiotemporal behavior for a spouting experiment, with jet velocity of approximately $v = 23$ m/s. Time evolves from left-to-right and top-to-bottom; each frame is separated in time by the camera frame rate of $1/30$ s.

C. Properties of the proper orthogonal decomposition

Since the kernel is Hermitian, $R(\mathbf{x}, \mathbf{y}) = R^*(\mathbf{y}, \mathbf{x})$, according to the Riesz theorem,³⁷ it admits a diagonal decomposition of the form

$$R(\mathbf{x}, \mathbf{y}) = \sum_{k=1}^N \lambda_k \Phi_k(\mathbf{x}) \Phi_k^*(\mathbf{y}). \tag{9}$$

This fact is particularly useful when finding the POD modes

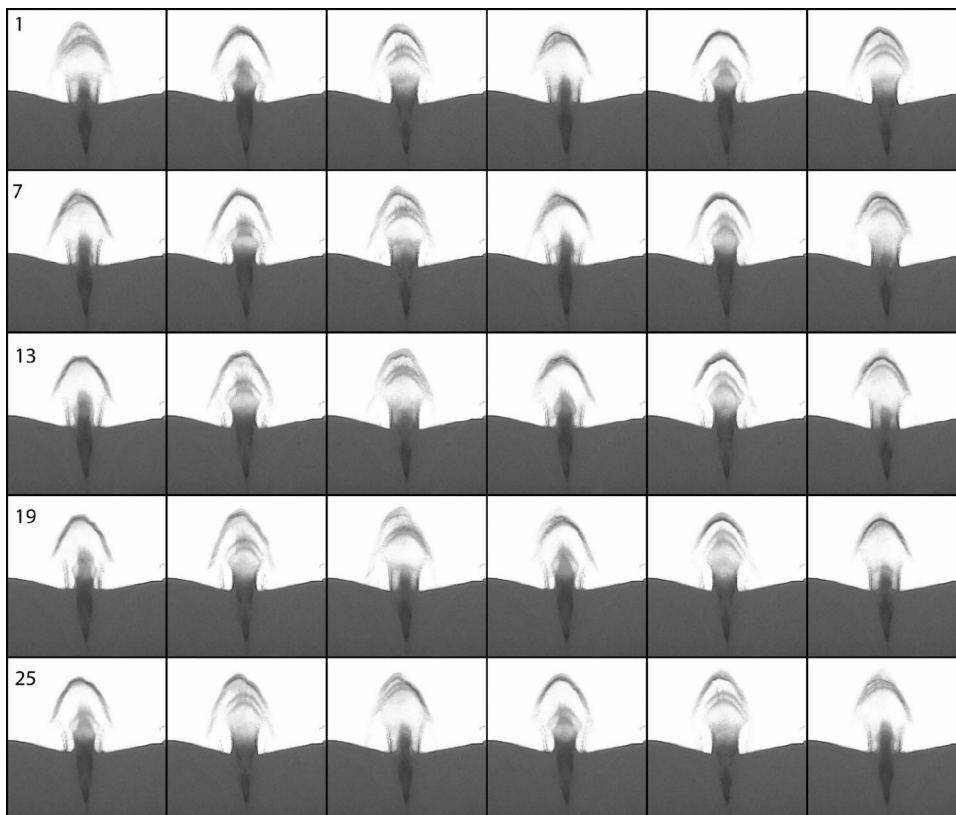


FIG. 3. Montage of spatiotemporal behavior for a spouting experiment, with jet velocity of approximately $v = 43$ m/s. Time evolves from left-to-right and top-to-bottom; each frame is separated in time by the camera frame rate of $1/30$ s.

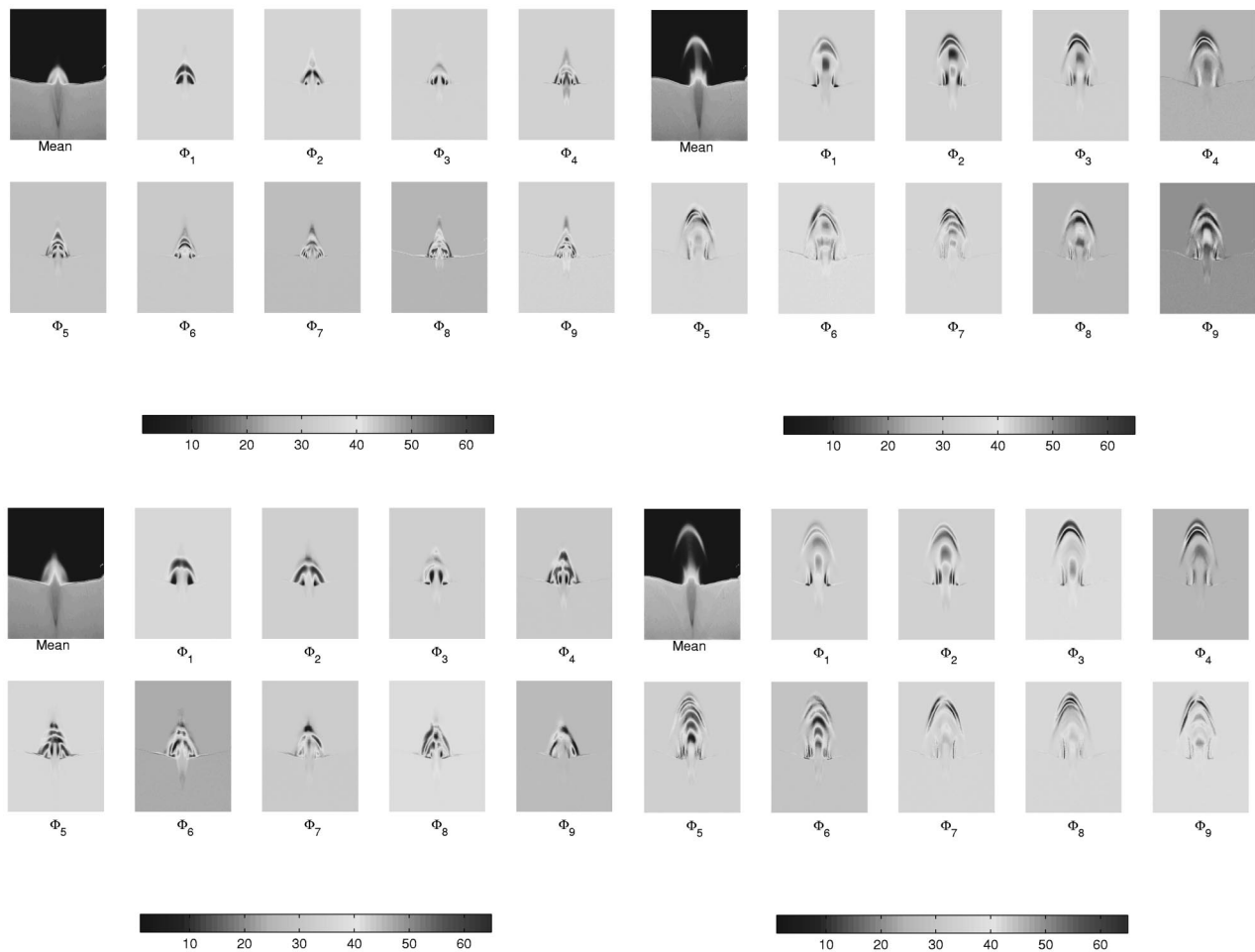


FIG. 4. POD spatial modes for spouting experiments, in which air flow is injected through a central nozzle inside a fluidized bed. Air flow velocity varies as follows: (top left) $v=23$ m/s; (top right) $v=31$ m/s; (bottom left) $v=39$ m/s; (bottom right) $v=43$ m/s.

analytically. They can be read off from the diagonal decomposition (9). Then the temporal coefficients, $a_k(t_i)$, are calculated by projecting the data set on each of the eigenfunctions,

$$a_k(t_i) = (u(\mathbf{x}, t_i), \Phi_k(\mathbf{x})), \quad i = 1, \dots, M. \quad (10)$$

It can be shown that both temporal coefficients and eigenfunctions are uncorrelated in time and space, respectively.^{31,38} In addition, the POD modes $\{\Phi_k(\mathbf{x})\}$ and the corresponding temporal coefficients, $\{a_k(t_i)\}$, satisfy the following orthogonality properties:

- (i) $\Phi_j^*(\mathbf{x})\Phi_k(\mathbf{x}) = \delta_{jk}$,
- (ii) $\langle a_j(t_i)a_k^*(t_i) \rangle = \delta_{jk}\lambda_j$,

where δ_{jk} represents the Kronecker delta function.

Property (ii) is obtained when the terms in the diagonal decomposition (9) are compared with the expression $R(\mathbf{x}, \mathbf{y}) = \sum \langle a_j(t_i)a_k^*(t_i) \rangle \Phi_j(\mathbf{x})\Phi_k^*(\mathbf{y})$. The non-negative and self-adjoint properties of $R(\mathbf{x}, \mathbf{y})$ imply that all eigenvalues are non-negative and can be ordered accordingly: $\lambda_1 \geq \lambda_2 \geq \dots \geq 0$. Statistically speaking, λ_k represents the variance of the data set in the direction of the corresponding POD mode, $\Phi_k(\mathbf{x})$. In physical terms, if u represents a com-

ponent of a velocity field, then λ_k measures the amount of kinetic energy captured by the respective POD mode, $\Phi_k(\mathbf{x})$. In this sense, the energy measures the contribution of each mode to the overall dynamics.

The total energy captured in a proper orthogonal decomposition of a numerical or experimental data set is defined as the sum of all eigenvalues,

$$E = \sum_{k=1}^M \lambda_k. \quad (11)$$

The relative energy captured by the k th mode, E_k , is defined by

$$E_k = \frac{\lambda_k}{\sum_{j=1}^M \lambda_j}. \quad (12)$$

Note that the cumulative sum of relative energies, $\sum E_k$, approaches one as the number of modes in the reconstruction increases to M .

D. Low-order model construction

Once the POD modes are computed, low-order models can be constructed via Galerkin methods, where a set of

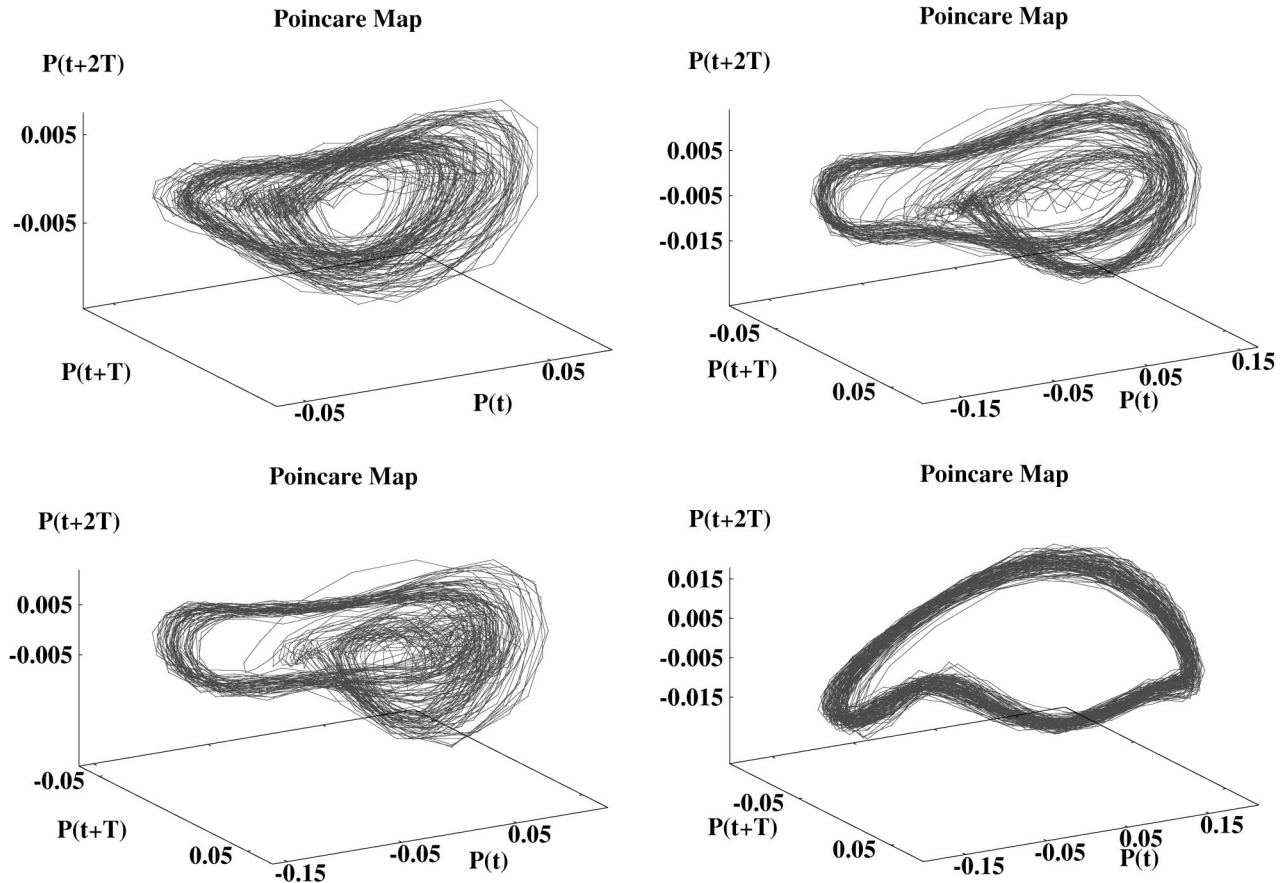


FIG. 5. Representative Poincaré maps obtained from pressure measurements of the spouting experiments described earlier. A period doubling bifurcation appears to occur when the air flow velocity decreases. Air flow velocity varies as follows: (top left) $v = 23$ m/s; (top right) $v = 31$ m/s; (bottom left) $v = 39$ m/s; (bottom right) $v = 43$ m/s.

PDEs are reduced to a smaller set of ordinary differential equations (ODEs). Briefly speaking, the main idea is as follows. Given a PDE model of the form

$$\frac{\partial u}{\partial t} = F(u),$$

the Galerkin procedure consists of using the POD decomposition of u shown in Eq. (2) to generate a reduced set of ODEs by solving

$$\left(\Phi_j, \sum_{k=1}^M \frac{da_k}{dt} \Phi_k(\mathbf{x}) - F \left(\sum_{k=1}^M a_k(t_i) \Phi_k(\mathbf{x}) \right) \right) = 0, \\ j = 1, \dots, M.$$

Note that the dependent variables of the set of ODEs are the POD amplitude coefficients. For further details, the reader is referred to Ref. 40.

V. RESULTS

Six experimental conditions are examined here. In each case, air was injected through the central nozzle but with different velocities varying from 23 to 43 m/s. This central jet produces a spatiotemporal flow pattern that is easier to analyze than that resulting from uniform excess gas flow through the distributor in which bubbles would be generated

fairly randomly throughout the bed. Figure 2 depicts the spatiotemporal evolution of the experiment at the lowest velocity examined, $v = 23$ m/s. An animation of these frames shows spatiotemporal behavior that is more visible on the bed-surface than in other regions of the bed, such as in the V-shape structure formed where the central gas jet becomes wide enough to be seen along the bed front surface. This suggests that the dynamics of the surface of the bed represents a global feature of the system, while the gas–solid motion inside the gas jet might be viewed more as a detailed feature of the system.

Figure 3 shows a similar montage of the spatiotemporal dynamics inside the bed, except that now the montage was recorded at the high end of the air velocity range, i.e., $v = 43$ m/s. At first glance, both cases appear to be similar. That is, the global feature of the bed dynamics is still captured, mainly, by the bed-surface behavior. To discern the differences, we apply next the proper orthogonal decomposition to all six cases.

In both of these sets of montages, one sees characteristic features of spouting beds. The injected air flows above the nozzle, and at a certain distance above the nozzle expands enough to impinge upon the walls of the shallow (1.9 cm) vessel used in this experiment. Particles are entrained in the jet and are ejected above the bed free surface into a fountain-

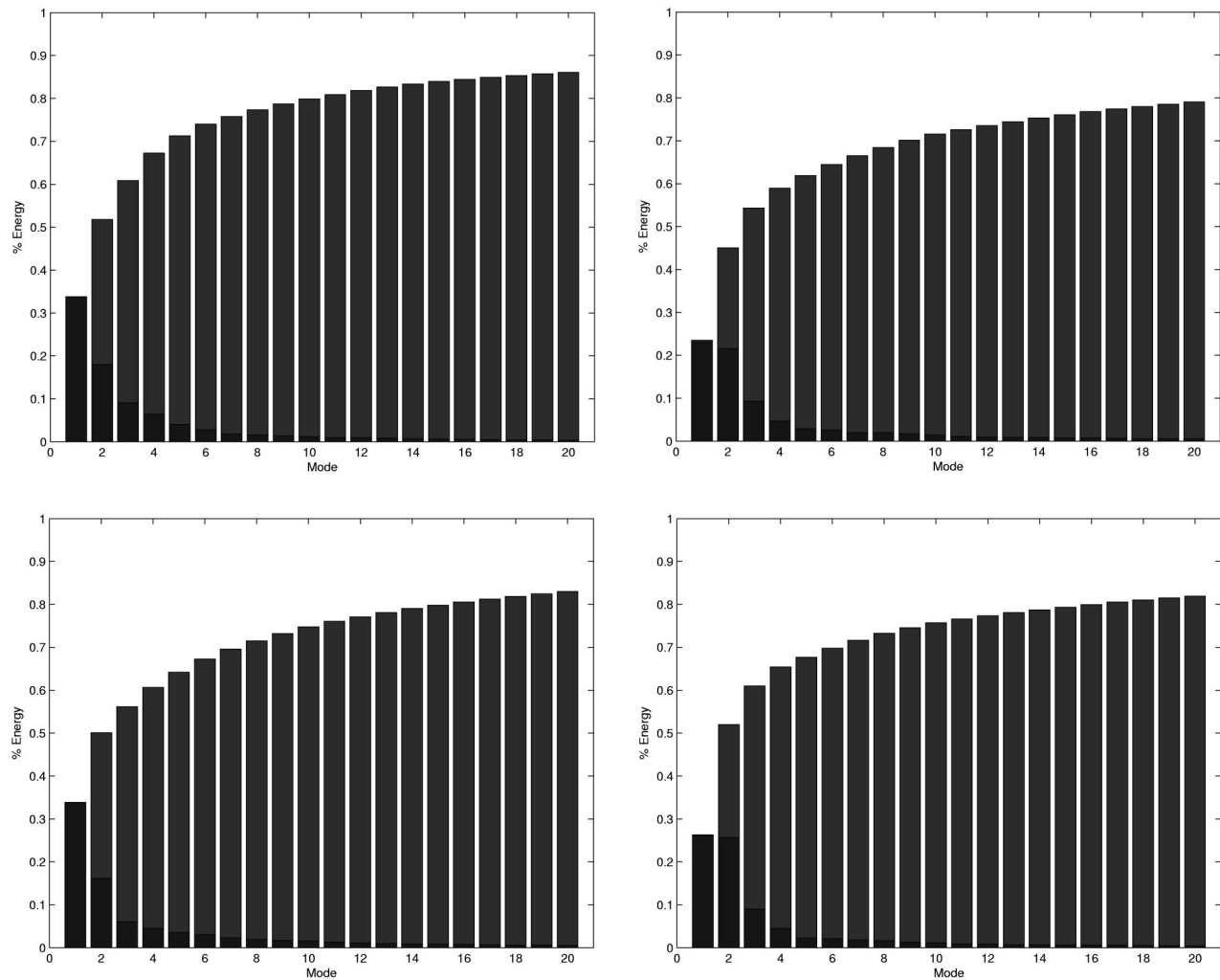


FIG. 6. POD energy spectrum for spouting experiments, in which air flow is injected through a central nozzle inside a fluidized bed. Air flow velocity varies as follows: (top left) $v=23$ m/s; (top right) $v=31$ m/s; (bottom left) $v=39$ m/s; (bottom right) $v=43$ m/s.

like structure, where they then rain back upon the bed surface. An interesting feature apparent in these montages is that the ejection of particles is not at a steady rate; otherwise, each video frame would be identical. Instead, there is a bit of slugging, as particles collapse periodically into the jet and then are entrained in bursts and ejected into the fountain; these bursts are viewed as waves in the fountain arch in the video frames. This variability in particle-ejection rates is a fundamental feature captured in spatiotemporal analysis.

Figure 4 shows the ten most energetic spatial modes (including the mean) that are obtained after applying the proper orthogonal decomposition (separately) to each of the six experimental data sets described earlier. Only the modes for four cases for $v=23$, $v=31$, $v=39$, and $v=43$ m/s are shown. In all six cases, the time-average captures the V-shape structure created by the central jet, while the remaining modes capture, mainly, the dynamics near the bed surface. Computer animations of the reconstructed flow with increasing numbers of POD modes, from one to 20 (including the time average), were performed and compared with the original simulations. Visual inspection of these animations reproduces the overall motion through the jet channel

structure, but the most visible changes appear near the bed surface. To further understand the nature of the dynamics near the V-jet, pressure measurements were recorded and analyzed. In particular, Fig. 5 shows the Poincaré maps (reconstructed phase space) that were obtained for the four cases of Fig. 4. The Poincaré maps suggest the existence of low-dimensional periodic behavior, which undergoes a period-doubling bifurcation as the air flow velocity decreases. Perhaps more sensitive recording equipment, with better temporal and spatial resolution, would be needed to study the fine-details of the gas-particle interactions inside the jet structure.

The POD energy spectrum for the above-discussed four cases is shown in Fig. 6. Note that in all cases approximately 80% of the original behavior is captured by the first 20 POD modes, including the time-average mode. Furthermore, Fig. 6 shows that when the air flow velocity is near $v=43$ m/s, the first two modes contain the same amount of POD energy, approximately 25%. Consequently, the contribution of these two modes to the reconstruction of the spatiotemporal dynamics is approximately the same. When the air velocity of the jet decreases, however, the POD energy in the second

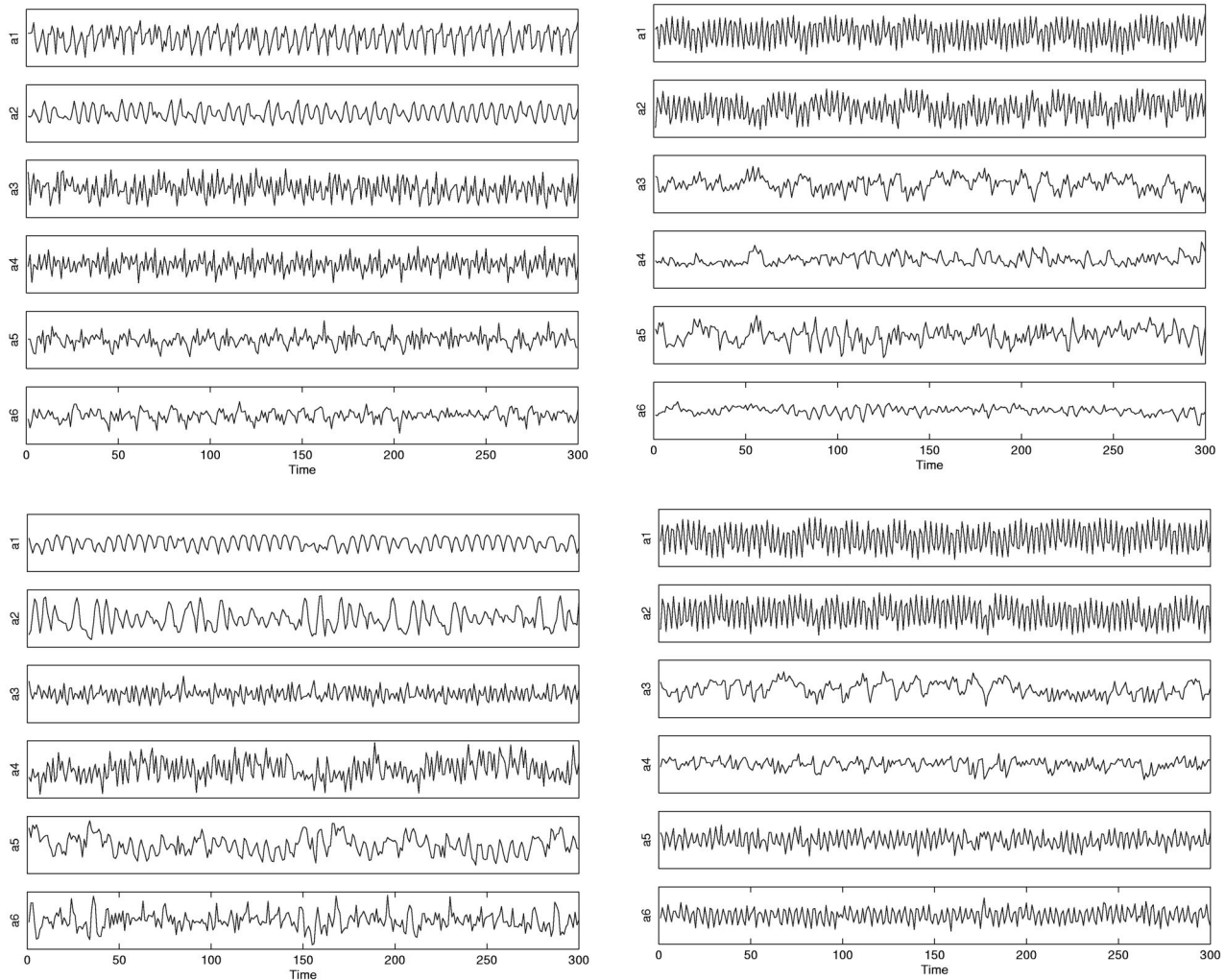


FIG. 7. POD amplitude coefficients for spouting experiments, in which air flow is injected through a central nozzle inside a fluidized bed. Air flow velocity varies as follows: (top left) $v = 23$ m/s; (top right) $v = 31$ m/s; (bottom left) $v = 39$ m/s; (bottom right) $v = 43$ m/s.

mode decreases. In fact, the overall energy spectrum appears to decay exponentially as the number of modes increases. Visual inspection of animations of the reconstructed dynamics reveals that high-energy modes contribute more to the fine details of the gas-particle interaction inside the jet structure, while low-energy modes reconstruct the behavior near the bed-surface.

Figure 7 shows the time-dependent amplitude coefficients associated with each of the POD modes shown previously in Fig. 4. In all six experimental cases, the time series produced by the first two amplitude coefficients (see Fig. 4) show a certain level of regularity. The frequency in the time series of the first two modes, however, increases as the air flow velocity increases. An animation of the reconstructed dynamics with the first two POD modes for $v = 23$ m/s, and corresponding amplitudes, shows the flow of air and entrained particles rising through the central jet channel and then producing a small splash of flow at the bed-surface. The cycle repeats, approximately, in a periodic fashion. The arch structure that is created above the bed surface appears to be almost symmetric with respect to the bed centerline. Similar results are obtained when the POD modes for $v = 43$ m/s are

used, though the splash at the bed surface is now larger. These observations suggest that the first two modes capture, mainly, the global features of the bed behavior and that these features could be reproduced by a low-dimensional deterministic model. Phase portraits of $a_1(t)$ vs $a_2(t)$ (not shown for brevity) also confirm the existence of low-dimensional behavior in the form of a limit cycle. Furthermore, the results also suggest that one could use the frequency of the amplitude coefficients for the first two POD modes to estimate the frequency of jet-pulsation dynamics.

As a final observation, note that in all four cases (actually all six cases), the time-average pattern (described by POD mode Φ_0) exhibits, approximately, a reflective symmetry (across a middle line running from top-to-bottom of the bed), which mimics the symmetry of the experimental system. As the number of modes increases, each individual reconstructed image shows less reflectional symmetry and closer resemblance to the bed-surface dynamics. More remarkable is the fact that the reflective symmetry can appear even when none of the time instantaneous snapshots shows this symmetry. Next we explain this point in more detail.

Suppose that the long-term behavior of the spouting ex-

periments is captured by an attractor, denoted by \mathcal{A} (see Ref. 41 for a precise definition). Assume that $\mathbf{g}(\mathbf{x}, t_i)$, $i = 1, \dots, M$ represents the scalar spatiotemporal measurements produced by our experimental work. In practice, as is the case of our POD implementation, one must first compute the time-average

$$\bar{\mathbf{g}}(\mathbf{x}) = \frac{1}{M} \sum_{i=1}^M g(\mathbf{x}, t_i),$$

in order to produce a new set of measurements, $u(\mathbf{x}, t_i) = g(\mathbf{x}, t_i) - \bar{\mathbf{g}}(\mathbf{x})$, with zero average. Let Γ denote the symmetry group of the system of interest. The symmetries of the attractor form a subgroup of Γ defined by

$$\Gamma_{(\mathcal{A})} = \{ \gamma \in \Gamma \mid \gamma \mathcal{A} = \mathcal{A} \}. \quad (13)$$

Dellnitz, Golubitsky, and Melbourne⁴² made the critical observation that symmetries of attractors of partial differential equations appear as symmetries of the time average, $\bar{\mathbf{g}}(\mathbf{x})$, independent of the symmetries of the instantaneous scalar field $g(\mathbf{x}, t_i)$. Unfortunately, the converse is not always true. The symmetries of the time average do not necessarily reflect the symmetries of the underlying attractor. This implies that reduced-order models obtained via Galerkin projections from partial differential equations onto POD modes might lead to ordinary differential equations with more symmetry than is present in an actual numerical simulation or experimental investigation.

VI. CONCLUSIONS AND FUTURE WORK

Experiments on a gas–particle fluidized bed were carried out to investigate the space–time dynamics of the spouting regime. A nozzle, located at the bottom-center of a uniformly fluidized bed, was used to inject air at several velocities to create a strong centerline jet and varying spout dynamics. The proper orthogonal decomposition method was then applied to video images of the experiments, recorded at 30 frames/s. Through the POD decomposition, we were able to identify and separate dominant spatial features from the temporal evolution of the system. The main dominant features, described by the POD modes with high levels of energy, capture the behavior of the flow near the bed surface, while low energy POD modes capture fine details of the gas–particle interaction near a V-shape central channel formed by the excess air flow. Furthermore, our results suggest that the time scales of variability within the jet, caused by pulsations of entrained particle densities, can be estimated from the frequency of the time series produced by the amplitude coefficients associated with the first two POD modes. Finally, our findings indicate that a low-dimensional model might be constructed via Galerkin projections from a suitable PDE model onto the POD modes. The low-dimensional model can be further used to study, at real-time speeds, the splash motion that is observed near the bed surface.

ACKNOWLEDGMENTS

We would like to thank the National Energy Technology Laboratory for their support for related work on fluidization

under Grant No. DE-FC26-00NT40903. We also wish to thank Madhava Syamlal and Sreekanth Pannala for many fruitful discussions.

- ¹D. P. Skrzyzce, K. Nguyen, and C. S. Daw, “Characterization of the fluidization behavior of different solid types based on chaotic time series analysis of pressure signals,” in Proceedings of the 12th International Conference on Fluidized Bed Combustion, San Diego, CA, 1993, pp. 155–156.
- ²C. S. Daw, C. E. A. Finney, M. Vasudevan, N. A. van Goor, K. Nguyen, D. D. Bruns, E. J. Kostelich, C. Grebogi, E. Ott, and J. A. Yorke, “Self-organization and chaos in a fluidized bed,” *Phys. Rev. Lett.* **75**, 2308–2311 (1995).
- ³C. S. Daw, W. F. Lawkins, D. J. Downing, and N. E. Clapp, Jr., “Complex characteristics of a complex gas–solids flow,” *Phys. Rev. A* **41**, 1179–1181 (1990).
- ⁴C. S. Daw and J. S. Halow, “Modeling deterministic chaos in gas-fluidized beds,” *AIChE Symp. Ser.* **88**, 61–69 (1992).
- ⁵C. S. Daw and J. S. Halow, “Evaluation and control of fluidization quality through chaotic time series analysis of pressure-drop measurements,” *AIChE Symp. Ser.* **89**, 103–122 (1993).
- ⁶J. C. Schouten and C. M. van den Bleek, “Chaotic hydrodynamics of fluidization: Consequences for scaling and modeling of fluidized bed reactors,” *AIChE Symp. Ser.* **88**, 70–84 (1992).
- ⁷J. C. Schouten, M. L. M. vander Stappen, and C. M. van den Bleek, “Deterministic chaos analysis of gas–solids fluidization,” in *Fluidization*, edited by O. E. Potter and D. J. Nicklin (Engineering Foundation, New York, 1992), Vol. VII, pp. 103–111.
- ⁸J. C. Schouten, M. L. M. vander Stappen, and C. M. van den Bleek, “The onset of deterministic chaos in gas–solids fluidization,” Proceedings of the Second International Conference on Micromechanics of Granular Media, 1993, pp. 395–400.
- ⁹M. L. M. vander Stappen, C. Schouten, and C. M. van den Bleek, “Application of deterministic chaos theory in understanding the fluid dynamic behavior of gas–solids fluidization,” *AIChE Symp. Ser.* **89**, 91–102 (1993).
- ¹⁰M. L. M. vander Stappen, C. Schouten, and C. M. van den Bleek, “The gas–solids fluidized bed as a spatio-temporal chaotic system,” *AIChE Symp. Ser.* **1**, 446–451 (1994).
- ¹¹M. L. M. vander Stappen, C. Schouten, and C. M. van den Bleek, “Chaotic hydrodynamics and scale-up of gas–solids fluidized beds: Using the Kolmogorov entropy for quantification,” in *Fluidization* (Engineering Foundation, New York, 1995), Vol. VII.
- ¹²R. Bakker, R. J. de Korte, J. C. Schouten, F. Takens, and C. M. van den Bleek, “Neural networks for prediction and control of chaotic fluidized bed hydrodynamics: A first step,” *Fractals* **5**, 525–530 (1997).
- ¹³R. Bakker, J. C. Schouten, M.-O. Coppens, F. Takens, and C. M. van den Bleek, “Robust learning of chaotic attractors,” in *Advances in Neural Information Processing Systems*, edited by S. A. Solla, T. K. Leen, and K.-R. Miller (MIT, Cambridge, 2000), Vol. 12, pp. 879–885.
- ¹⁴R. Bakker, J. C. Schouten, C. L. Giles, F. Takens, and C. M. van den Bleek, “Learning chaotic attractors by neural networks,” *Neural Comput.* **12**, 2355–2383 (2000).
- ¹⁵L. Fan and C. Zhu, *Principles of Gas–Solid Flows* (Cambridge University Press, New York, 1997).
- ¹⁶S. K. Garg and J. W. Pritchett, “Dynamics of gas-fluidized beds,” *J. Appl. Phys.* **46**, 4493–4500 (1975).
- ¹⁷D. Gidaspow, *Multiphase Flow and Fluidization* (Academic, Boston, 1994).
- ¹⁸D. Gidaspow and B. Etehadieh, “Fluidization in two-dimensional beds with a jet. 2. Hydrodynamic modeling,” *Ind. Eng. Chem. Fundam.* **22**, 193–201 (1983).
- ¹⁹A. Boemer, H. Qi, and U. Renz, “Eulerian simulation of bubble formation at a jet in a two-dimensional fluidized bed,” *Int. J. Multiphase Flow* **5**, 927–944 (1997).
- ²⁰R. Clift and J. R. Grace, “Bubble interaction in fluidized beds,” *Int. J. Multiphase Flow* **105**, 14–27 (1985).
- ²¹D. Gera and M. Gautam, “Variation of throughflow velocity in a 2-d rising bubble,” *Powder Technol.* **79**, 257–263 (1994).
- ²²D. Gera and M. Gautam, “Bubble rise velocity in two-dimensional fluidized beds,” *Powder Technol.* **84**, 283–285 (1995).
- ²³F. A. Zenz, “Bubble formation and grid design,” *Inst. Chem. Eng. Symp. Ser.* **30**, 136–139 (1968).

- ²⁴D. Kunii and O. Levenspiel, *Fluidization Engineering* (Butterworth-Heinemann, London, 1991).
- ²⁵J. Bridgwater, in *Fluidization*, 2nd ed. (Academic, London, 1985), Chap. 6.
- ²⁶K. B. Mathur, in *Fluidization*, edited by J. F. Davidson and D. Harrison (Academic, New York, 1971).
- ²⁷J. C. Russ, *The Image Processing Handbook*, 2nd ed. (CRC Press, Ann Arbor, 1995).
- ²⁸K. Karhunen, "Zur spektraltheorie stochasticher," *Ann. Acad. Sci. Fenn., Ser. A 1*, 34 (1946).
- ²⁹M. Loeve, *Probability Theory* (Van Nostrand, New York, 1955).
- ³⁰G. Berkooz, P. Holmes, and J. L. Lumley, "The proper orthogonal decomposition in the analysis of turbulent flows," *Annu. Rev. Fluid Mech.* **25**, 539–575 (1993).
- ³¹P. Holmes, J. L. Lumley, and G. Berkooz, *Turbulence, Coherent Structures, Dynamical Systems and Symmetry* (Cambridge University Press, New York, 1996).
- ³²J. L. Lumley, "The structure of inhomogeneous turbulent flows," in *Atmospheric Turbulence and Radio Wave Propagation*, edited by A. M. Yaglom and V. I. Tatarski (Nauka, Moscow, 1967), pp. 167, 168.
- ³³M. D. Graham, S. L. Lane, and D. Luss, "Proper orthogonal decomposition analysis of spatiotemporal temperature patterns," *J. Phys. Chem.* **97**, 889–894 (1993).
- ³⁴R. Preisendorfer, *Principal Component Analysis in Meteorology and Oceanography*, edited by C. Mobley (Elsevier Amsterdam, 1988).
- ³⁵K. W. Pratt, *Digital Image Processing*, 2nd ed. (Wiley, New York, 1991).
- ³⁶C. L. Pettit and P. S. Beran, "Reduced-order modeling for flutter prediction," in the 41st AIAA/ASCE/AHS/ASC Structural, Structural Dynamics and Materials Conference, Atlanta, GA, 2000.
- ³⁷F. Riesz and B. Sz.-Nagy, *Functional Analysis* (Dover, New York, 1990).
- ³⁸L. Sirovich, "Turbulence and the dynamics of coherent structures," *Q. Appl. Math.* **5**, 561–590 (1987).
- ³⁹D. E. Stewart and Z. Leyk, "Meschach: Matrix computations in C," in CMA Proceedings No. 32, Canberra, Australia, 1994. Australian National University.
- ⁴⁰C. A. J. Fletcher, *Computational Galerkin Methods* (Springer, New York, 1984).
- ⁴¹J. K. Hale, *Ordinary Differential Equations* (Wiley, New York, 1980).
- ⁴²M. Dellnitz, M. Golubitsky, and M. Nicol, "Symmetry of attractors and the Karhunen–Loève decomposition," in *Trends and Perspectives in Applied Mathematics*, edited by L. Sirovich (Springer, New York, 1994), pp. 73–108.